Journal of Applied Electrochemistry (2006) 36:265–275
DOI 10.1007/s10800-005-9080-0

Theoretical investigation of steady state multiplicities in solid oxide fuel cells*

MICHAEL MANGOLD*, MYKHAYLO KRASNYK and KAI SUNDMACHER
Max-Planck-Institut für Dynamik komplexer technischer Systeme, Sandtorstr. 1, 39106, Magdeburg, Germany
*(*author for correspondence +49-391-6110-513, E-mail: mangold@mpi-magdeburg.mpg.de)*

Received 1 December 2004; accepted in revised form 19 April 2005

Key words: bifurcation analysis, fuel cells, modelling, nonlinear dynamics, SOFC

Abstract

The nonlinear steady state behaviour of solid oxide fuel cells (SOFCs) is investigated. It is found that the temperature dependence of the electrolyte conductivity has a very strong influence on the occurrence of multiple steady states, instabilities and the formation of hot spots. Two correlations from the literature for the electrolyte conductivity are studied in a lumped model and in a 1D spatially distributed model of a SOFC. The cases of galvanostatic operation, potentiostatic operation, and operation under a constant ohmic load are considered. The lumped model possesses a unique steady state under galvanostatic operation and up to three steady states under potentiostatic operation or under constant load. In the distributed model, three steady states may coexist under galvanostatic operation and up to five under potentiostatic operation.

List of Symbols

B	width of cell (m)
c_P	molar heat capacity (J mol^{-1} K^{-1})
C^{SE}	coefficient in Equation (24) (Ω^{-1} m^{-1})
c_t	total gas concentration (mol m^{-3})
d	thickness of electrodes (m)
D_{eff}	diffusion coefficient (m^2 s^{-1})
E	activation energy (J mol^{-1})
E^{SE}	coefficient in Equation (24) (J mol^{-1})
F	Faraday constant (96485 C mol^{-1})
$\Delta_R G$	free enthalpy of reaction at T_{ref} (J mol^{-1})
H	height of gas channels (m)
$\Delta_R H$	heat of reaction (J mol^{-1})
i	current density (A m^{-2})
I	total cell current (A)
$\dot{n}$	molar flow (mol s^{-1})
p	pressure (Pa)
R	ohmic resistance (Ω)
R	gas constant (8.314 J mol^{-1} K^{-1})
$\Delta_R S$	entropy of reaction at T_{ref} (J mol^{-1} K^{-1})
t	time (s)
U^{Cell}	cell voltage (V)
y_j	molar fraction
z	space coordinate (m)

Greek symbols

α	heat transfer coefficient (W m^{-2} K^{-1})
$\beta_{1/2}$	coefficients in Equation (23)
γ	pre-exponential kinetic factor (A m^{-2})
η	overpotential (V)
θ	charge transfer coefficient
λ	heat conductivity of the solid (W m^{-1} K^{-1})
ν	stoichiometric coefficient
ρ	resistivity (Ω m)
ρ^S	density of the solid (kg m^{-3})
Φ	electrical potential (V)

Superscripts

A	anode
C	cathode
E	electrolyte
S	solid

1. Introduction

Dynamic instabilities in chemical and electrochemical systems have been investigated over the last decades [1, 2]. It has been shown that in electrical and electrochemical systems multiplicities and oscillations can be caused by a negative differential resistance, i.e. by an electrical resistance decreasing with increasing current [3–5]. This

---

* Paper originally given at the CHISA Congress, Prague, August 2004.

property is found for quite different physical systems like gas discharge systems [6] or semiconductor devices [7, 8], and for various electrochemical reactions like the electro-oxidation of CO [9] or H_2 [10]. However, very little work has been done on nonlinear effects in fuel cells. Ertl and coworkers studied oscillations in electrochemical methanol oxidation and pointed out a possible relevance for direct methanol fuel cells [11]. Datta and coworkers have investigated instabilities in proton exchange membrane fuel cells (PEMFCs) caused by the presence of CO in theoretical and experimental studies [12, 13]. Recently, Benziger and coworkers showed that in autohumidified PEMFCs bistabilities can occur due to an autocatalytic effect: Water formed in the electrochemical reaction increases the conductivity of the polymer membrane, hence accelerates the reaction, and increases the water concentration further, leading to a so-called 'wet spot' [14–16]. To our knowledge, there are hardly any publications available on instabilities and multiplicities in high temperature fuel cells. In previous work [17], we showed that in high temperature fuel cells there may exist a thermokinetic equivalent to the autocatalytic wet spot formation in PEMFCs: The electrolyte connecting the electrodes of a high temperature fuel cell possesses an electrical conductivity that increases with temperature. Therefore, a local temperature increase may lead to higher current density, which intensifies the local electrochemical reaction rate, produces more heat and in the end may result in the formation of a hot spot. With the help of an idealised dimensionless fuel cell model it could be demonstrated in [17] that this effect can lead to steady state multiplicities and complex spatial patterns.

The purpose of the present contribution is to extend the investigation to a more detailed model of a solid oxide fuel cell (SOFC) that uses experimentally validated reaction kinetics and model parameters from the literature. Two versions of the model, a spatially distributed one and a simplified lumped version, will be derived in the next section. In Section 3 and 4, the steady state and dynamic behaviour of the two model versions will be investigated by a bifurcation analysis.

When analysing the nonlinear behaviour of a fuel cell, one is always confronted with the problem that a stand-alone fuel cell is not of much technical use but should be studied in connection with some external electrical circuit. On the other hand, it is the objective of this paper to identify nonlinear effects actually caused by the phenomena inside the cell and not by the properties of an external device. To overcome this difficulty, this work considers three idealising modes of operation: (1) the case of perfect galvanostatic operation of the fuel cell, (2) the case of perfect potentiostatic operation, and (3) the case of a constant external ohmic resistance (see Figure 1). The first two cases are taken from the way fuel cells are characterised in a laboratory. In laboratory experiments, the fuel cell is often connected to a measuring instrument that either provides a constant current (galvanostat) or a constant voltage (potentiostat). This is achieved by control mechanisms inside the measuring instrument, which usually work so well that the cell current may be considered as an independent parameter for galvanostatic operation and that the cell voltage may be considered as an independent parameter for potentiostatic operation. In the case of galvanostatic operation, the fuel cell responds to the fixed cell current with a certain cell voltage. In the case of potentiostatic operation, it responds to the fixed cell voltage with a certain cell current. The third case is a simple example of the use of the cell as an electrical power source. Here, the resistance of the external load is a free control parameter, while cell current and cell voltage are coupled by Ohm's law.

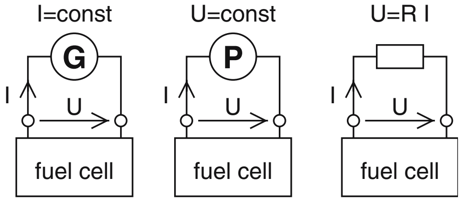

Fig. 1. Operation modes of a fuel cell considered in this work: (1) connection to a perfect galvanostat; (2) connection to perfect potentiostat; (3) connection to an ohmic resistance.

2. Modelling

Two SOFC models of different degrees of detail are used in the following. The first is spatially one-dimensional and describes a counter-current cell as shown in Figure 2. The complete set of model equations is listed in Appendix A. The model parameters used in the simulations are listed in Table 1.

The main model assumptions are as follows:

The gases in the gas channels on the anode and on the cathode side behave ideally. A plug flow through the gas channels is considered. A pressure drop along the gas channels as well as pressure changes with time are neglected.

The mass transport through the electrodes to the reactive layer is limited by a mass transfer resistance. This is included in the model by a linear driving force approach.

The material transported through the porous electrodes to the reactive catalyst layer is consumed immediately in the electrochemical reactions, i.e. the electrodes storage capacity for mass is negligible, because the electrodes are very thin.

The electrochemical reactions

$$H_2 + O^{2-} \rightarrow H_2O + 2e^- \tag{1}$$

and

$$\frac{1}{2}O_2 + 2e^- \rightarrow O^{2-} \tag{2}$$

are assumed to take place on the anode and cathode sides, respectively. The anodic and cathodic reaction kinetics are of Butler–Volmer type and are taken from [18].

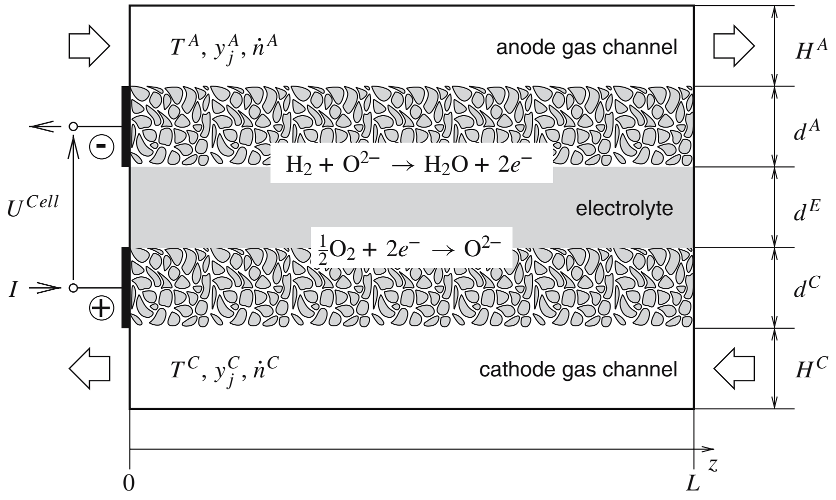

Fig. 2. Scheme of the counter-current SOFC considered in the spatially distributed model.

Table 1. Model parameters used in the simulations, if not given differently in the text

$B = 0.04$ m	a	$p = 100000$ Pa	
$c_{P,H2} = 30$ J mol^{-1} K^{-1}		$\Delta_R\ S = -57$J mol^{-1} K^{-1}	
$c_{P,H\_2O} = 44$ J mol^{-1} K^{-1}		$T_{in}^{A/C} = 1000$ K	
$c_{P,N2} = 34$ J mol^{-1} K^{-1}		$T_{ref} = 1300$ K	
$c_{P,O2} = 36$ J mol^{-1} K^{-1}		$y_{H2,in}{}^A = 0.9$	
$C^{SE} = 2.8\times\ 10^8$ K Ω^{-1} m^{-1}	b	$y_{H\_2O,in}{}^A = 0.1$	
$d^A = 10^{-4}$ m	a	$y_{N2,in}{}^C = 0.8$	
$d^C = 0.5\times\ 10^{-4}$ m	a	$y_{O2,in}{}^C = 0.2$	
$d^E = 1.8\times\ 10^{-4}$ m	a	$\alpha = 25$ W m^{-2} K^{-1}	
$D_{eff}^A = 3.5\times 10^{-5}$ m^2 s^{-1}	a	$\beta_1 = 3.34\times\ 10^{-4}\Omega^{-1}$ m^{-1}	a
$D_{eff}^C = 7.3\times\ 10^{-6}$ m^2 s^{-1}	a	$\beta_2 = 1.03\times\ 10^4$ K	a
$E^A = 140000$ J mol^{-1}	a	$\gamma^A = 5.7\times 10^7$ A m^{-2}	a
$E^C = 160000$ J mol^{-1}	a	$\gamma^C = 7\times\ 10^9$ A m^{-2}	a
$E^{SE} = 96900$ J mol^{-1}	b	$\theta_a^A = 2$	a
$\Delta_R\ G = -175933$ J mol^{-1}		$\theta_c^A = 1$	a
$H^A = 10^{-3}$ m		$\theta_a^C = 1.4$	a
$H^C = 10^{-3}$ m		$\theta_c^C = 0.6$	a
$\Delta_R\ H = -241830$ J mol^{-1}		$\lambda = 0.7$W m^{-1} K^{-1}	
$L = 0.4$ m		$\rho^A = 1.5\times\ 10^{-7}\Omega$ m	a
$\dot{n}_{in}^A = 1.39 \times 10^{-3}$ mol s^{-1}	a	$\rho^C = 4.2\times\ 10^{-8}\ \Omega$ m	a
$\dot{n}_{in}^C = 3.8 \times 10^{-2}$ mol s^{-1}	a	$(\rho\ c_P)^S = 10^6$ J m^{-3} K^{-1}	

[a] source [18]; [b]source: [19]

Transport of electrical charge is considered in the electrodes in the direction of the *z*-coordinate, and in the electrolyte in the direction perpendicular to the *z*-coordinate. The capacities of the double layers are neglected, as they are usually very small and as the interest of this paper focuses on the slower temperature dynamics of the cell.

Following [18], the conductivity of the electrodes is considered as invariant with temperature, whereas a temperature dependence of the electrolyte electrical conductivity is taken into account. As will be shown later, this temperature dependence has a very strong impact on the nonlinear behaviour of the cell and can cause multiple steady states. Therefore, two different approaches for the electrolyte conductivity are used. The first variant is an Arrhenius type expression taken from [18]. The second variant is a modified Arrhenius correlation described in [19]. Figure 3 shows that, while the absolute values of the two correlations differ, the temperature dependencies are very similar.

Energy transport between the gaseous and the solid phases occurs due to convective heat transfer proportional to a heat transfer coefficient α, and due to the enthalpy transport coupled to the mass fluxes. It is assumed that fluxes from the gas to the solid phase have the temperature of the gas and vice versa. On the anode side, the transport of water from the anode to the anode gas channel has to be taken into account by a term in the temperature equation of the anode gas channel. Because there is no transport of material from the cathode to the cathode gas channel, a corresponding term is missing in the equation for the cathode gas temperature.

A pseudo-homogeneous energy balance is used for the anode, the cathode, and the electrolyte, assuming a high heat transfer and hence a vanishing temperature difference between the three solid phases. The resulting temperature equation for the pseudo-homogeneous solid phase contains source terms due to the heat of reaction, the conversion of internal energy into electrical energy, the heat generation due to ohmic losses in the electrodes, the heat transport by conduction in the solid phase, and the heat exchange between the gas channels and the solid parts of the cell.

The model is completed by an additional equation describing the external electrical circuit that depends on the considered case of operation.

The spatially distributed model is rather complex and requires numerical analysis. Before carrying out such a numerical study, it seems worthwhile doing some qualitative considerations based on a simplified model. The simplified model results from the spatially distributed model by the following additional model assumptions: Spatial gradients are neglected, temperatures, concentrations, and potentials are constant across the whole cell area. The composition and temperature in the gas channels are considered as constant parameters,

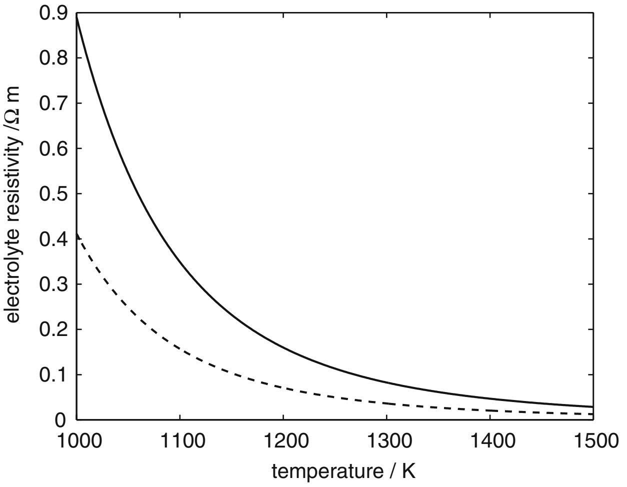

Fig. 3. Temperature dependence of the electrolyte resistivity according to model variant I [18] (solid line) and model variant II [19] (dashed line).

e.g. due to high flow rates in the channels. The mass transfer resistance between gas channels and solid as well as the electrical resistance of the metallic electrodes are neglected. These assumptions lead to the model whose equations are listed in Appendix B. The model consists of the temperature Equation (34), of three implicit algebraic Equations (31–33) for the anodic and cathodic overpotentials and the total cell voltage, and of one of the Equations (28–30) depending on the considered mode of operation.

3. Analysis of the lumped model

The purpose of this section is to determine conditions, where the simplified lumped model can possess multiple co-existing steady states. The easiest way to do this is by comparing the heat sinks and sources on the right-hand side of (34) for different cell temperatures – a method that has been in use for exothermic CSTRs for a long time [20, 21]. The steady state version of (34) can be written as

$$0 = Q_P(T^S) - Q_R(T^S) \tag{3}$$

$$Q_P(T^S) := \left(\frac{(-\Delta_R H)}{2F} - \left(\Phi^C - \Phi^A\right) + \frac{c_{P,\mathrm{H_2}}}{2F}\left(T^A - T^S\right) + \frac{c_{P,\mathrm{O_2}}}{4F}\left(T^C - T^S\right) \right) \frac{I(T^S)}{LB} \tag{4}$$

$$Q_R(T^S) := 2\alpha T^S - \alpha(T^A + T^C) \tag{5}$$

The function Q_R describes the removal of heat by exchange between the solid and the gas channels. It is linear in T^S with a positive slope. The function Q_P comprises all terms on the right-hand side of (34) that depend on T^S in a nonlinear way and describes the heat production. The evaluation of Q_P requires the solution of the implicit algebraic Equations (31–33) in combination with one of the Equations (28–30) for a given value of T^S. A steady state temperature is reached, if Q_P equals Q_R. This condition can be evaluated graphically.

Figure 4 shows examples of this construction for different modes of operation of the cell.

In case (1) of galvanostatic operation, the cell current is considered as a constant model parameter, and Q_P is evaluated for varying values of T^S. It is found that only one intersection point is possible between the heat removal line Q_R, which increases with T^S, and the heat production curve Q_P, which decreases monotonically with T^S. Hence, the steady state is always unique for this model in the case of galvanostatic operation. The physical reason is that mainly the reaction kinetics contain the nonlinear terms of the model. Keeping the cell current constant means to fix the reaction rates of the cell and to suppress most of its nonlinear behaviour. However, it will be shown later that this conclusion holds for the lumped model only. In the spatially distributed model multiplicities can also occur for galvanostatic operation, as this model possesses additional degrees of freedom.

In case (2) of potentiostatic operation, the cell voltage is kept constant, while the solid temperature T^S is varied. The resulting heat production curve has the sigmoidal shape typical of exothermic reactors. The heat removal line can intersect this curve up to three times. Hence, up to three steady state solutions can coexist, of which the middle one is unstable, whereas the upper and the lower one are statically stable solutions. This qualitative result is obtained for both model variants used for the electrolyte conductivity. However, if the electrolyte conductivity is assumed to be temperature independent (dotted line in the middle diagram of Figure 4), then the heat production curve changes much less with temperature, and the range of model parameters where multiplicities can occur becomes much smaller. From this it can be concluded that the variance of the electrical conductivity with temperature plays a crucial role for the occurrence of multiple steady states in a SOFC.

The third case considered is the operation of the cell with a constant ohmic resistance (lower diagram of Figure 4), where neither cell current nor cell voltage are independent parameters, but are coupled by Ohm's law. The qualitative behaviour in this operation mode is the same as under potentiostatic operation. Up to three steady states are found to coexist.

These qualitative results can be validated by a numerical bifurcation analysis of the lumped model (31–34) using some standard continuation package. Here, the continuation methods contained in the simulation tool DIVA [22] are applied. For potentiostatic operation, the cell voltage can be used as the independent bifurcation parameter. The model shows a hysteresis behaviour

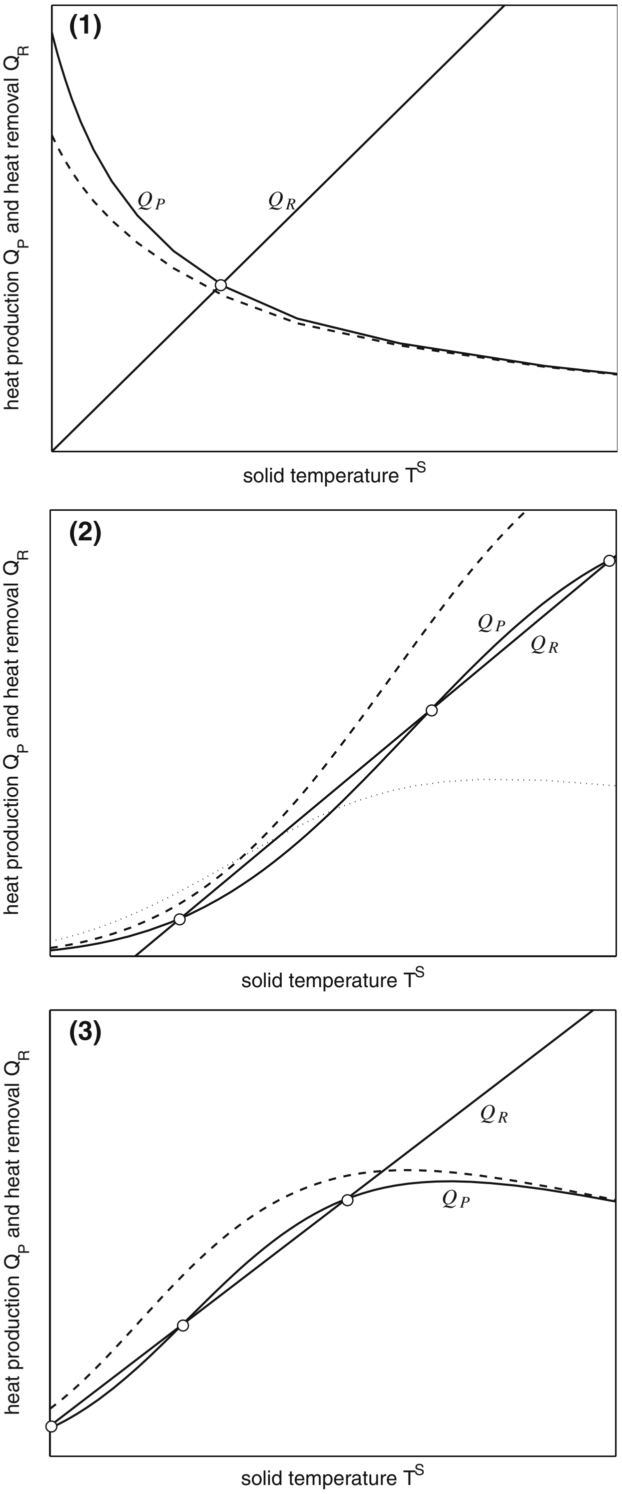

Fig. 4. Qualitative analysis of steady state multiplicities in the lumped model; (1) galvanostatic operation; (2) potentiostatic operation; (3) operation under a constant ohmic load; solid lines $= Q_P$ for model variant I, dashed line $= Q_P$ for model variant II, dotted line in (2) $= Q_P$ assuming a temperature independent electrolyte conductivity; white circles indicate intersections between heat removal line Q_R and heat production curve Q_P for model variant II, which define the steady state temperatures.

with a low-temperature branch of stable steady states and a co-existing stable high-temperature branch (Figure 5).

If the cell is initially operated at the low-temperature branch and the cell voltage is reduced below the value given by the limit point LP1, then the low temperature solution vanishes and the cell jumps to the high-temperature branch in a strong and sudden temperature rise. Obviously, the temperatures on the high-temperature solution branch are extremely high, above realistic operation temperatures of a SOFC and beyond the limit, where the model is still valid. However, the lower limit point LP1 lies in a region of reasonable operation conditions, i.e. the stability loss and the sudden temperature increase occur under conditions relevant for SOFC operation, even if the ignited steady state is never reached in reality. The characteristic cell voltage vs. cell current in Figure 5(b) has a rather unusual nonmonotonic shape. This shape is caused by the temperature dependence of the electrolyte electrical conductivity, as can be seen from a comparison to a model with constant conductivity. The thin lines in Figure 5 show the results, if the electrolyte conductivity

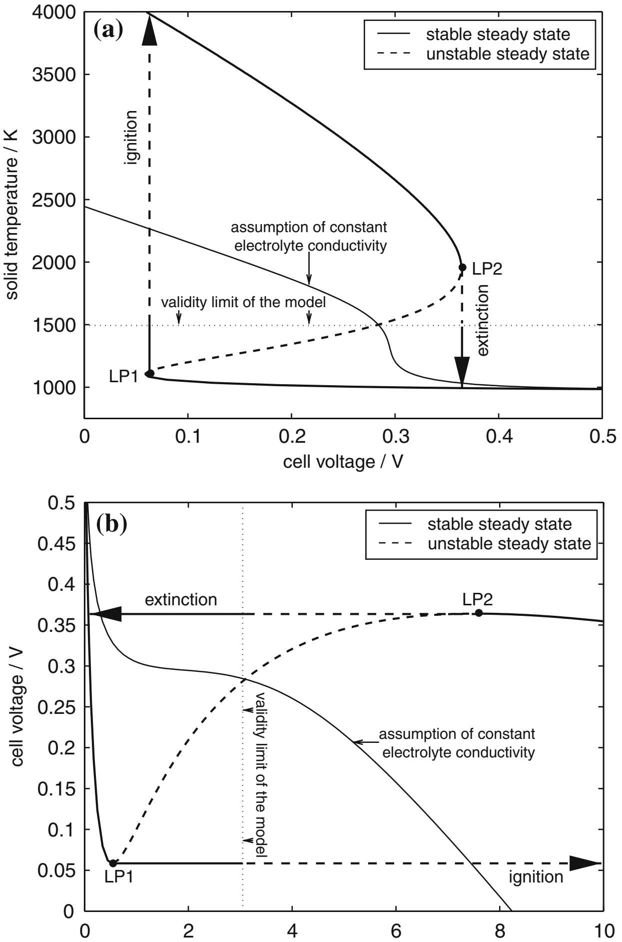

Fig. 5. Bifurcation analysis of the lumped model (model variant I) for case (2) of potentiostatic operation; cell voltage U^{Cell} is used as bifurcation parameter; $T^A = T^C = 980$ K; (a) solid temperature vs. cell voltage; (b) cell voltage vs. average current density $I/L/B$; thin lines in (a) and (b) show the system behaviour, if the electrolyte conductivity is assumed to be temperature independent.

is assumed to be constant at a value obtained from (23) for $T^S = 1500$ K. In this case, the cell voltage decreases monotonically with the cell current.

The operation of the cell under a ohmic load is studied by using the resistance of the external load as a bifurcation parameter. As can be seen in Figure 6(a), a reduction of the load resistance below the value given by the lower limit point leads to sudden temperature increase and to the transient of the cell to a new steady state on the high temperature branch. A subsequent increase in load resistance above the value given by the upper limit point results in a drop in cell temperature to the low-temperature branch of steady state solutions. The corresponding voltage vs. current characteristic in Figure 6(b) has exactly the same shape as for the potentiostatic operation, Figure 5(b). Coupling the cell voltage and cell current via an ohmic resistor only affects the stability of the solutions.

In Figures 7 and 8, additional model parameters and operational conditions are included in the analysis of multiple steady states. Potentiostatic operation is considered. The figures show multiplicity regions in a parameter plane defined by the parameters cell voltage and gas temperature. Operation conditions, where multiple steady states exist, lie within the shaded areas. The boundaries of the shaded areas are formed by limit points. For example, the limit points LP1 and LP2 from Figure 5 are found in Figure 7 as intersection points of the dashed line $T^A = T^C = 980$ K and of the boundary of the multiplicity region for $\alpha = 25$ W m^{-2} K^{-1}. If the gas temperatures are increased, then the limit points and the region of steady states move towards higher values of cell voltage. At the same time, the distance between the limit points decreases, i.e. the range of values of the cell voltage, where multiplicities exist, becomes smaller for higher gas temperatures. In Figure 7, the two limit points coincide for $\alpha = 25$ W m^{-2} K^{-1} at gas temperatures of about 1250 K and a cell voltage of about 0.4 V. For gas temperatures above 1250 K, the multiplicities

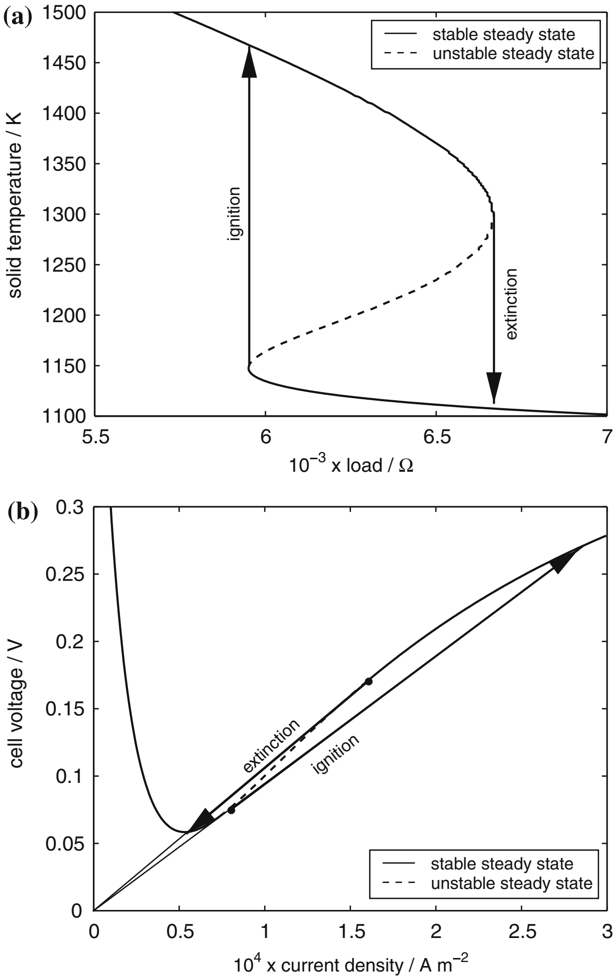

Fig. 6. Bifurcation analysis of the lumped model (model variant I) for case (3) of operation under a constant ohmic load; the load resistance is used as bifurcation parameter; $T^A = T^C = 980$ K; (a) solid temperature vs. cell voltage; (b) cell voltage vs. average current density $I/L/B$.

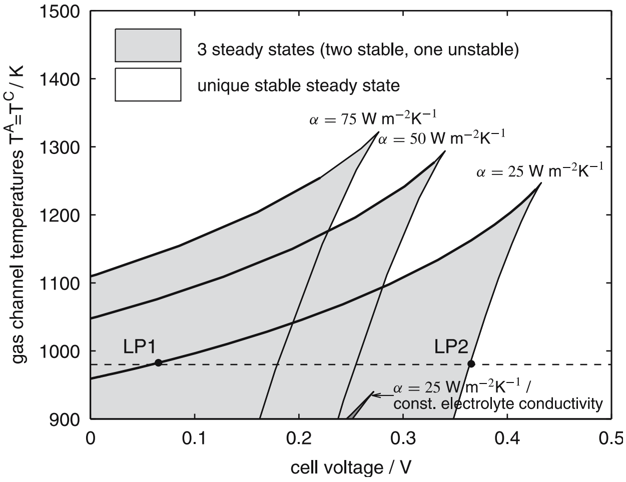

Fig. 7. Multiplicity regions of the lumped model (model variant I) for the case of potentiostatic operation; bold lines indicate limit points with a solid temperature below 1500 K.

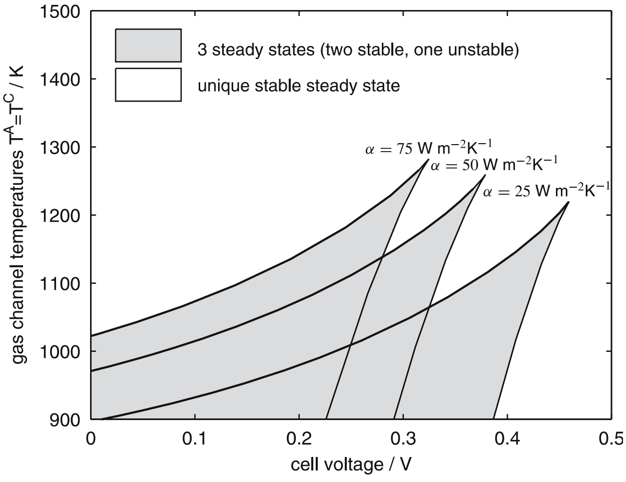

Fig. 8. Multiplicity regions of the lumped model (model variant II) for the case of potentiostatic operation; bold lines indicate limit points with a solid temperature below 1500 K.

vanish completely. Figures 7 and 8 also show that the heat transfer coefficient between gas and solid phases α only affects the quantitative behaviour of the model, but hardly the qualitative results. Increasing the heat transfer coefficient only shifts the multiplicity region towards smaller values of cell voltage and towards higher gas temperatures, but cannot destroy it. Furthermore, it is found that model variant I (Figure 7) and model variant II (Figure 8) hardly differ with respect to the multiplicity region. However, the result changes strongly, if a temperature independent conductivity of the electrolyte is assumed. In this case, the multiplicity region shrinks to a tiny area in Figure 7, indicating again, that the occurrence of multiple steady states is mainly caused by the varying electrolyte conductivity.

4. Analysis of the spatially distributed model

The investigations of the previous section are now extended to the spatially distributed model. Additional phenomena taken into account in this more detailed model are the varying composition and temperature of the anode and cathode gases along the flow channels, the mass transfer resistance between gas and solid phases, and the spatial dependence of the electrical potentials and the solid temperature. For the numerical analysis, the model is spatially discretised on an equidistant grid of 400 grid points using the method of lines. In order to get a spatially discretised system with differential index one, the time derivative of the total concentration in (8) is eliminated by using the thermal equation of state (15) and the temperature Equations (10, 12). Ordinary differential equations in space for the molar flow rates $\dot{n}^A, \dot{n}^C$ result. The simulator DIVA is used for dynamical simulations and numerical bifurcation analysis.

Figure 9 shows multiplicity regions of the distributed model under potentiostatic operation and can be seen in connection with results for the lumped model in Figure 7.

Because the temperature of the gas channels are no longer model parameters in the detailed model, the inlet temperatures of the gases are treated as the second bifurcation parameter instead. The resulting multiplicity region is similar to the multiplicity region of the lumped model. However, the additional degrees of freedom of the spatially distributed model are reflected by the coexistence of up to five steady states, whereas in the lumped model only three coexisting steady states are found. Figure 10 gives a closer look on the multiplicity region. It was obtained by varying the cell voltage under potentiostatic operation for constant inlet gas temperatures of 1000 K, i.e. by moving along the lower border of Figure 9.

For a given cell voltage of e.g. 0.28 V the cell can be in five different steady states 1–5 with different cell temperatures and different cell currents. Further, the figure shows that multiple steady states can also coexist for a given cell current, e.g. states i,ii, and iii for a average current density of 2500 A m^{-2}, whereas the steady states of the lumped model under galvanostatic operation are always unique. The reason for this difference is that galvanostatic operation of the distributed model only fixes the overall cell current, but allows differences in spatial distribution of the current density that are not taken into account in the lumped model. The physical mechanism behind the galvanostatic multiplicities is the interaction between the heat production by the electrochemical reaction and the temperature dependence of the electrolyte electrical conductivity. This interaction may narrow down the charge transport through the electrolyte to a small portion of the electrode area, resulting in a channel of high current density and a hot spot. The coexisting spatial profiles of

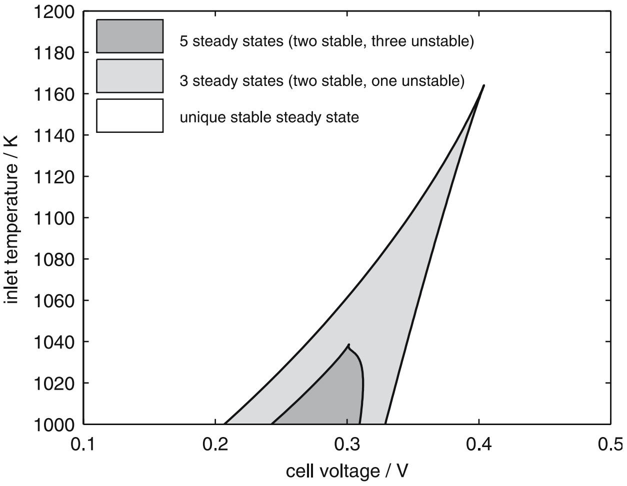

Fig. 9. Multiplicity regions of the spatially distributed model (model variant I) for case (2) of potentiostatic operation.

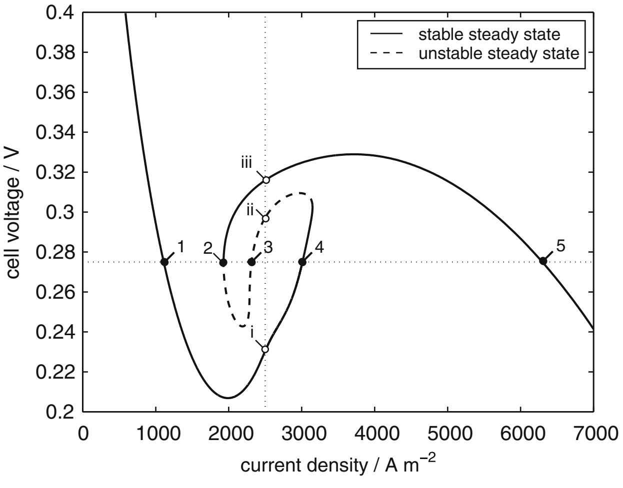

Fig. 10. Cell voltage vs. average current density $I/L/B$ of the spatially distributed model (model variant I, $T_{in}^A = T_{in}^C = 1000$ K); 1–5 are coexisting steady states under potentiostatic operation; (i)–(iii) are coexisting steady states under galvanostatic operation; stability information in the figure refers to galvanostatic operation.

the temperature and the current density in Figure 11 illustrate this effect.

In the case of solution (i), the current density along the space coordinate varies comparatively weakly, and the maximum temperature is rather low. In the case of solution (iii), the electrochemical reaction and the production of heat and electrical current concentrates on the left boundary region of the cell, where a high temperature peak forms. The unstable solution (ii) lies in the middle between the two stable solutions. A transient from solution (i) to solution (iii) can be reached by a sufficiently strong local disturbance of the cell temperature. A local temperature increase reduces the local resistivity of the electrolyte and hence increases the local current density and the local reaction rate. This leads to an increase in local heat production, to a further temperature rise and to a further reduction in local resistivity. This destabilising effect is counteracted by heat transport in the axial direction due to heat conduction. A new equilibrium, solution (iii), is reached when the temperature gradients are sufficiently steep that enough heat can be removed from the hot zone by conduction.

The coexistence of the spatially more homogeneous solution of type (i) and the hot spot solution of type (iii) is limited to a certain range of average cell current densities as follows from Figure 10. Under the conditions shown in Figure 10 the type (i) solution is unique for cell current densities below 2000 A m^{-2}, whereas for current densities above 3500 A m^{-2} solely the hot spot solution of type (iii) exists.

The importance of the temperature dependence of the electrolyte electrical conductivity is confirmed by a dynamic simulation shown in Figure 12. The transient response to an increase in cell current is considered assuming (a) a constant, temperature independent electrolyte conductivity and (b) a temperature dependent conductivity according to Equation (23) (model variant I). In case (a), the higher cell current leads to a moderate rise in cell temperature. In case (b), the combined increase in temperature and electrical conductivity in the cell left boundary region results in a channelling of the current density and in a hot spot of very high temperature.

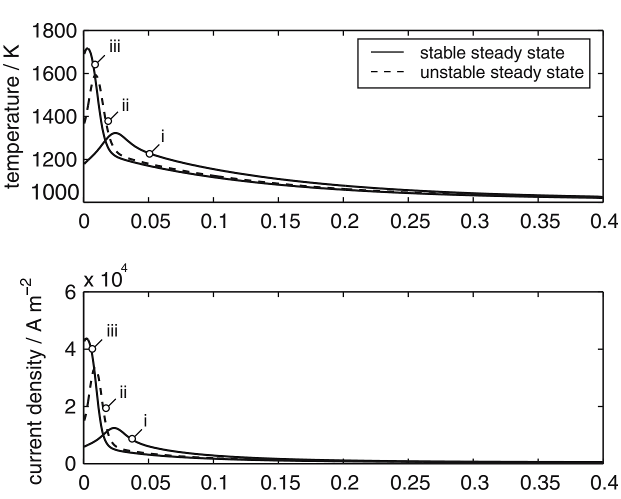

Fig. 11. Coexisting spatial profiles of the temperature and the current density of the distributed model under case (1) of galvanostatic operation (model variant I, $T_{in}^{A} = T_{in}^{C} = 1000$ K, $I/L/B = 2500$ A m^{-2}).

5. Conclusions

Temperature control is crucial in the operation of high temperature fuel cells. The prediction and avoidance of local over-temperatures requires a thorough understanding of the various processes of heat production and heat transport interacting in a fuel cell. From the analysis of classical chemical fixed bed reactors, a number of mechanisms are known to be responsible for the formation of hot spots, e.g. the decrease in feed temperature or interaction between exothermic and endothermic reactions [23, 24]. These mechanisms are

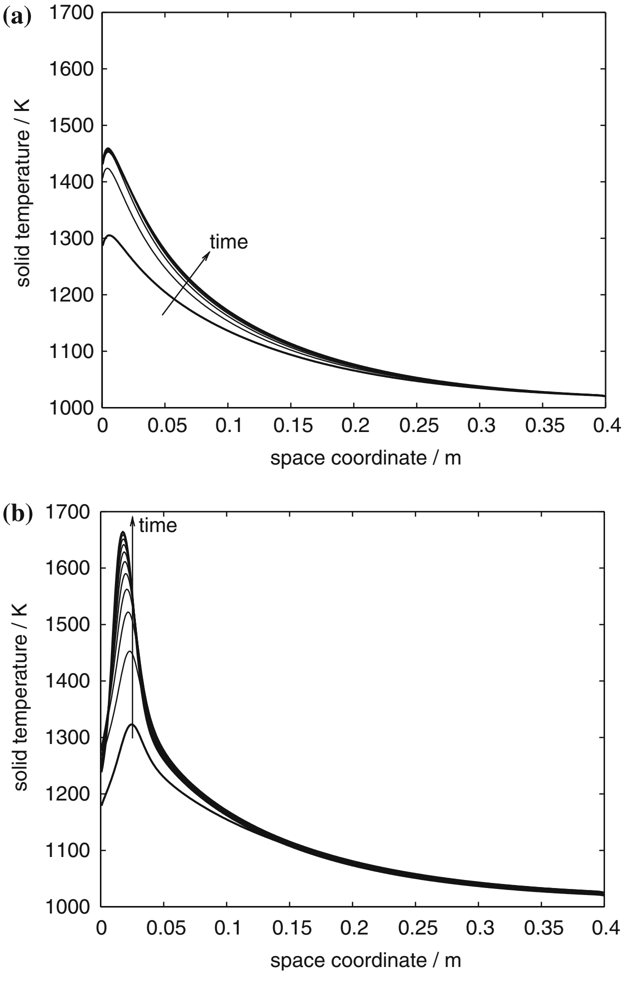

Fig. 12. Transient response of the spatially distributed model to an increase of the cell current density $I/L/B$ from 2500 A m^{-2} to 3200 A m^{-2} at time $t = 0$; spatial profiles of the solid temperature at $t = 0$, 10,...,100 s; (a) assumption of a temperature independent electrolyte conductivity; (b) electrolyte conductivity according to Equation (23).

also relevant for high temperature fuel cells. However, this work indicates that in high temperature fuel cells an additional effect has to be taken into account that is not present in conventional fixed bed reactors. This effect is the temperature dependence of the electrical conductivity of the electrolyte. The mobility of the ions in the electrolyte and hence the conductivity increase with increasing temperature. Therefore, a local temperature disturbance has a destabilising effect on the fuel cell: a temperature increase at one point leads to a higher conductivity and a higher current density at this point; this results in a stronger local heat production due to the exothermic electrochemical reaction that increases the temperature further. The consequence is the occurrence of an S-shaped current-potential curve, i.e. of multiple steady states coexisting under certain operation conditions. The existence of multiplicities depends mainly on the qualitative property of a negative differential resistance of the system and less on the quantitative type of temperature dependence of the electrolyte conductivity. This is shown by the comparison between two different correlations for the conductivity in this work and by the results of a previous publication [17].

This study considers three modes of operation of the fuel cell: the connection to a perfect galvanostat, to a perfect potentiostat, and to an ohmic resistance. If spatial gradients in the fuel cell are neglected, multiple steady states exist only in the last two cases. However, if a spatially distributed model is used, then co-existing steady states are also found for a fixed cell current. The reason for this behaviour is that a fixed cell current only determines the total heat generated by the chemical reaction, but allows for degrees of freedom with respect to the spatial distribution of the heat generation.

The models studied here only show static multiplicities but no dynamic instabilities like e.g. autonomous oscillations. The reason is that there is only one dominating time constant in the considered systems that is given by the thermal storage capacity of the solid. It can be expected that oscillations may occur if several fuel cells are coupled thermally by heat exchange. The found multiple steady states appear mainly for high current densities. As future fuel cell development aims at intensifying the process and increasing the power density and current density, the problem of multiplicities combined with hot spot formation may become more important in the future. The studies in this work show that bifurcation analysis can help to detect thermal instabilities in high temperature fuel cells and to modify the process in such a way, that the region of multiplicities is shifted out of the area of usual operation conditions.

This contribution only covers one part of a fuel cell system. Additional complexities will arise, if peripheral systems and control circuits like e.g. the controlled supply of fuel gas are also taken into account. External electrical loads with a more complicated behaviour than the simple idealised examples used here may cause additional instabilities. The influence of such effects will be the focus of future work, but is excluded from this contribution. A thorough nonlinear analysis of a complete fuel cell system seems possible only if the relevant effects inside the cell are well understood. The present work is intended to contribute to this understanding.

Acknowledgements

The authors thank Dipl.-Ing. (FH) Richard Hanke and Dipl.-Ing. Barbara Munder for helpful discussions.

Appendix A. Model equations of the spatially distributed model

- Anode and cathode gas channels:

– Component material balances:

$$\frac{\partial}{\partial t}\left(y_j^{A/C} c_t^{A/C}\right) = \mp \frac{1}{H^{A/C}B}\frac{\partial \dot{n}_j^{A/C}}{\partial z} + \frac{\nu_j^{A/C}}{H^{A/C}}\frac{i}{2F} \tag{6}$$

$$y_j^A(0,t) = y_{j,in}^A(t), \quad y_j^C(L,t) = y_{j,in}^C(t) \tag{7}$$

($j = H_2$, H_2O on anode side, and $j = N_2$, O_2 on cathode side)

– Total material balance:

$$\frac{\partial c_t^{A/C}}{\partial t} = \mp \frac{1}{H^{A/C}B}\frac{\partial \dot{n}^{A/C}}{\partial z} + \frac{1}{H^{A/C}}\sum_j \nu_j^{A/C}\frac{i}{2F} \tag{8}$$

$$\dot{n}^A(0,t) = \dot{n}_{in}^A(t), \quad \dot{n}^C(L,t) = \dot{n}_{in}^C(t) \tag{9}$$

– Temperature equation on anode side

$$\begin{aligned} c_t^A c_P^A \frac{\partial T^A}{\partial t} = &-\frac{\dot{n}^A}{H^A B} c_P^A \frac{\partial T^A}{\partial z} + \frac{i}{2F}\frac{c_{P,H_2O}}{H^A}\left(T^S - T^A\right) \\ &+ \frac{\alpha}{H^A}\left(T^S - T^A\right) \end{aligned} \tag{10}$$

$$T^A(0,t) = T_{in}^A(t) \tag{11}$$

– Temperature equation on cathode side

$$c_t^C c_P^C \frac{\partial T^C}{\partial t} = \frac{\dot{n}^C}{H^C B} c_P^C \frac{\partial T^C}{\partial z} + \frac{\alpha}{H^C}\left(T^S - T^C\right) \tag{12}$$

$$T^C(L,t) = T_{in}^C(t) \tag{13}$$

– Specific molar heat capacity:

$$c_P^{A/C} = \sum_j y_j^{A/C} c_{P,j} \tag{14}$$

– Thermal equation of state:

$$c_t^{A/C} = \frac{p}{RT^{A/C}} \tag{15}$$

- Solid phase:

– - Component material balances:

$$0 = D^{A/C}_{eff} c_t \frac{y_j^{A/C} - y_j^S}{d^{A/C}} + \nu_j^{A/C} \frac{i}{2F} \tag{16}$$

– Anodic reaction kinetics:

$$\begin{aligned} i = {} & \gamma^A y^S_{H_2} y^S_{H_2O} \exp\left(-\frac{E^A}{RT^S}\right) \\ & \left\{\exp\left(\theta_a^A \frac{F}{RT^S}\eta^A\right) - \exp\left(-\theta_c^A \frac{F}{RT^S}\eta^A\right)\right\} \end{aligned} \tag{17}$$

– Cathodic reaction kinetics:

$$\begin{aligned} i = {} & \gamma^C {y^S_{O_2}}^{0.25} \exp\left(-\frac{E^C}{RT^S}\right) \\ & \left\{\exp\left(\theta_a^C \frac{F}{RT^S}\eta^C\right) - \exp\left(-\theta_c^C \frac{F}{RT^S}\eta^C\right)\right\} \end{aligned} \tag{18}$$

– Charge balances in the electrodes:

$$\frac{\partial}{\partial z}\left(\frac{d^{A/C}}{\rho^{A/C}} \frac{\partial \Phi^{A/C}}{\partial z}\right) = \pm i \tag{19}$$

$$\Phi^A(0,t) = 0, \quad \frac{Bd^C}{\rho^C} \frac{\partial \Phi^C}{\partial z}\bigg|_{0,t} = I, \quad \frac{\partial \Phi^A}{\partial z}\bigg|_{L,t} = \frac{\partial \Phi^C}{\partial z}\bigg|_{L,t} = 0 \tag{20}$$

– Voltage drop in the electrolyte:

$$\begin{aligned} U^{Cell} &= \Phi^C(0,t) - \Phi^A(0,t) \\ &= U^0(T^S) - \eta^A - \eta^C - \rho^E(T^S) d^E i \end{aligned} \tag{21}$$

– Open circuit voltage:

$$\begin{aligned} U^0(T^S) = -\frac{1}{2F}\Bigg(& \Delta_R G - \Delta_R S(T^S - T_{ref}) \\ & + RT^S \ln \frac{y^A_{H_2O}}{y^A_{H_2} {y^C_{O_2}}^{0.5}} \Bigg) \end{aligned} \tag{22}$$

– Electrical conductivity of the electrolyte:

$$\text{Variant I}: \quad \rho^E = \frac{1}{\beta_1} \exp\left(\frac{\beta_2}{T^S}\right) \tag{23}$$

$$\text{Variant II}: \quad \rho^E = \frac{T^S}{C^{SE}} \exp\left(\frac{E^{SE}}{RT^S}\right) \tag{24}$$

– Temperature equation for the solid phase:

$$\begin{aligned} & (d^A + d^E + d^C)(\rho c_P)^S \frac{\partial T^S}{\partial t} \\ & = \left(\frac{(-\Delta_R H)}{2F} - (\Phi^C - \Phi^A)\right) i \\ & \quad + \frac{d^A}{\rho^A}\left(\frac{\partial \Phi^A}{\partial z}\right)^2 + \frac{d^C}{\rho^C}\left(\frac{\partial \Phi^C}{\partial z}\right)^2 \\ & \quad + (d^A + d^E + d^C)\lambda \frac{\partial^2 T^S}{\partial z^2} \\ & \quad + \left(\alpha + \frac{i}{2F} c_{P,H_2}\right)(T^A - T^S) \\ & \quad + \left(\alpha + \frac{i}{4F} c_{P,O_2}\right)(T^C - T^S) \end{aligned} \tag{25}$$

$$-\lambda \frac{\partial T^S}{\partial z}\bigg|_{0,t} = \alpha\left(T_{amb} - T^S(0,t)\right) \tag{26}$$

$$\lambda \frac{\partial T^S}{\partial z}\bigg|_{L,t} = \alpha\left(T_{amb} - T^S(L,t)\right) \tag{27}$$

– Depending on the mode of operation, one of the following three equations is used for describing the external electrical circuit:

– Case (1): galvanostatic operation

$$I = \text{const.} \tag{28}$$

– Case (2): potentiostatic operation

$$U^{Cell} = \text{const.} \tag{29}$$

– Case (3): operation with an external ohmic load

$$U^{Cell} = RI \tag{30}$$

Appendix B. Model equations of the lumped model

- Anodic reaction kinetics:

$$\begin{aligned} \frac{I}{LB} = {} & \gamma^A y^S_{H_2} y^S_{H_2O} \exp\left(-\frac{E^A}{RT^S}\right) \\ & \left\{\exp\left(\theta_a^A \frac{F}{RT^S}\eta^A\right) - \exp\left(-\theta_c^A \frac{F}{RT^S}\eta^A\right)\right\} \end{aligned} \tag{31}$$

- Cathodic reaction kinetics:

$$\begin{aligned} \frac{I}{LB} = {} & \gamma^C {y^S_{O_2}}^{0.25} \exp\left(-\frac{E^C}{RT^S}\right) \\ & \left\{\exp\left(\theta_a^C \frac{F}{RT^S}\eta^C\right) - \exp\left(-\theta_c^C \frac{F}{RT^S}\eta^C\right)\right\} \end{aligned} \tag{32}$$

- Voltage drop in the electrolyte:

$$U^{\text{Cell}} = \Phi^C - \Phi^A = U^0(T^S) - \eta^A - \eta^C - \rho^E(T^S)d^E\frac{I}{LB} \tag{33}$$

- Temperature equation for the solid phase:

$$\begin{aligned}(d^A + d^E + d^C)(\rho c_P)^S\frac{dT^S}{dt} = {}& \\ & \left(\frac{(-\Delta_R H)}{2F} - \left(\Phi^C - \Phi^A\right)\right)\frac{I}{LB} \\ & + \left(\alpha + \frac{c_{P,\mathrm{H_2}}}{2F}\frac{I}{LB}\right)\left(T^A - T^S\right) \\ & + \left(\alpha + \frac{c_{P,\mathrm{O_2}}}{4F}\frac{I}{LB}\right)\left(T^C - T^S\right)\end{aligned} \tag{34}$$

- External load described by Equations (28), (29), or (30)

References

1. J. Hudson and T. Tsotsis, *Chem. Eng. Sci.* **49** (1994) 1493.
2. L. Pismen, *Chem. Eng. Sci.* **35** (1980) 1950.
3. M. Koper and J. Sluyters, *J. Electroanal. Chem.* **371** (1994) 149.
4. K. Krischer, N. Mazouz and G. Flätgen, *J. Phys. Chem. B* **104** (2000) 7545.
5. N. Mazouz and K. Krischer, *J. Phys. Chem. B* **104** (2000) 6081.
6. H.-G. Purwins, C. Radehaus, T. Dirksmeyer, R. Dohmen, R. Schmeling and H. Willebrand, *Phys. Lett. A* **125** (1987) 92.
7. G. Hüpper, G.E. Schöll and L. Reggiani, *Solid-State Electronics* **32** (1989) 1787.
8. F.-J. Niedernostheide (ed.), *Nonlinear Dynamics and Pattern Formation in Semiconductors and Devices* (Springer, Berlin, 1995).
9. M. Koper, T. Schmidt, N. Marković and P. Ross, *J. Phys. Chem. B* **105** (2001) 8381.
10. H. Varela and K. Krischer, *Catal. Today* **70** (2001) 411.
11. J. Lee, C. Eickes, M. Eiswirth and G. Ertl, *Electrochim. Acta* **47** (2002) 2297.
12. J. Zhang and R. Datta, *Electrochem. Solid State Lett.* **7** (2004) A37.
13. J. Zhang, J. Fehribach and R. Datta, *J. Electrochem. Soc.* **151** (2004) A689.
14. J. Benziger, E. Chia, E. Karnas, J. Moxley, C. Teuscher and I. Kevrekidis, *AIChE J.* **50** (2004) 1889.
15. E. Chia, J. Benziger and I. Kevrekidis, *AIChE J.* **50** (2004) 2320.
16. J. Moxley, S. Tulyani and J. Benziger, *Chem. Eng. Sci.* **58** (2003) 4705.
17. M. Mangold, M. Krasnyk and K. Sundmacher, *Chem. Eng. Sci.* **59** (2004) 4869.
18. P. Costamagna and K. Honegger, *J. Electrochem. Soc.* **145** (1998) 3995.
19. B. Munder, Y. Ye, L. Rihko-Struckmann and K. Sundmacher: Submitted to Catalysis Today (2005).
20. F. Liljenroth, *Chem. Metallurg. Eng.* **19** (1918) 287.
21. C. van Heerden, *Chem. Eng. Sci.* **7** (1958) 133.
22. M. Mangold, A. Kienle, K. Mohl and E. Gilles, *Chem. Eng. Sci.* **55** (2000) 441.
23. G. Kolios, J. Frauhammer and G. Eigenberger, *Chem. Eng. Sci.* **55** (2000) 5945.
24. D. Luss, *Industr. Eng. Chem. Res.* **36** (1997) 2931.